

Occluded Prohibited Items Detection: An X-ray Security Inspection Benchmark and De-occlusion Attention Module

Yanlu Wei*

weyanlu@buaa.edu.cn
State Key Lab of Software Development Environment, Beihang University

Yuqing Ma

mayuqing@buaa.edu.cn
State Key Lab of Software Development Environment, Beihang University

Renshuai Tao*

rstao@buaa.edu.cn
State Key Lab of Software Development Environment, Beihang University

Libo Zhang

libo@iscas.ac.cn
Institute of Software Chinese Academy of Sciences

Zhangjie Wu

zhangjiewu@buaa.edu.cn
State Key Lab of Software Development Environment, Beihang University

Xianglong Liu†

xlliu@buaa.edu.cn
State Key Lab of Software Development Environment, Beihang University

ABSTRACT

Security inspection often deals with a piece of baggage or suitcase where objects are heavily overlapped with each other, resulting in an unsatisfactory performance for prohibited items detection in X-ray images. In this work, first, we contribute a high-quality dataset named OPIXray, each of which is annotated manually by professional inspectors from an international airport. To the best of our knowledge, this is the first dataset specifically designed for object detection in security inspection. Second, we propose a De-occlusion Attention Module (DOAM) that can be inserted as a plug-and-play module into most detectors, aiming at detecting occluded prohibited items in X-ray images. Central to DOAM are EIEM, RIAM and HAG. EIEM and RIAM capture edge information and region information of the prohibited item respectively, and HAG generates the attention map by hybridizing the two feature maps generated by EIEM and RIAM to serve a refined feature map to a general detector. We evaluate our method on the OPIXray dataset and compare it to several baselines, including popular methods for detection and attention mechanisms. As is shown from the results, our proposed method significantly outperforms existing models. The data and code are released at <https://github.com/OPIXray-author/OPIXray>.

CCS CONCEPTS

• Computing methodologies → Object detection; Computer vision.

KEYWORDS

object detection, security inspection, X-ray images, occlusion.

*Both authors contributed equally to this research.

†Corresponding author.

Permission to make digital or hard copies of all or part of this work for personal or classroom use is granted without fee provided that copies are not made or distributed for profit or commercial advantage and that copies bear this notice and the full citation on the first page. Copyrights for components of this work owned by others than ACM must be honored. Abstracting with credit is permitted. To copy otherwise, or republish, to post on servers or to redistribute to lists, requires prior specific permission and/or a fee. Request permissions from permissions@acm.org.

MM '20, October 12–16, 2020, Seattle, United States

© 2020 Association for Computing Machinery.

ACM ISBN 978-x-xxxx-xxxx-x/YY/MM...\$15.00

<https://doi.org/10.1145/nnnnnnnn.nnnnnnnn>

ACM Reference Format:

Yanlu Wei, Renshuai Tao, Zhangjie Wu, Yuqing Ma, Libo Zhang, and Xianglong Liu. 2020. Occluded Prohibited Items Detection: An X-ray Security Inspection Benchmark and De-occlusion Attention Module. In *Proceedings of the 28th ACM International Conference on Multimedia (MM '20), October 12–16, 2020, Seattle, United States*. ACM, New York, NY, USA, 10 pages. <https://doi.org/10.1145/nnnnnnnn.nnnnnnnn>

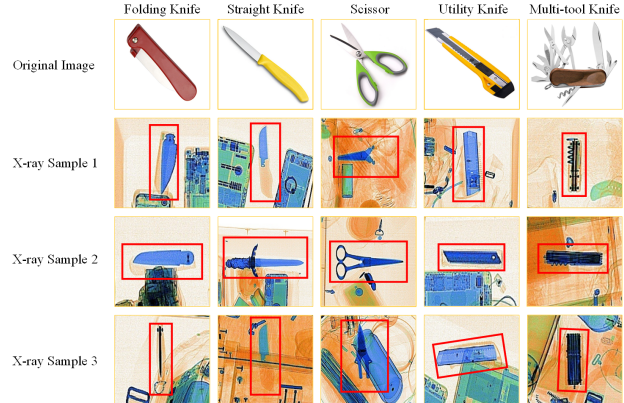


Figure 1: Samples of the five categories of cutters and corresponding X-ray images.

1 INTRODUCTION

With the increasing crowd density in public transportation hubs, security inspection has become more and more important in protecting public space from safety threatening, such as terrorism. Security inspection usually adopts X-ray scanners to find whether there is any prohibited item in luggage, such as bags or suitcases. However, in this scenario, objects are randomly stacked and heavily overlapped with each other, leading to object occlusion challenge. As a result, after a long time localizing prohibited items in large amounts of complex X-ray images without distraction, security inspectors struggle to accurately detect all the prohibited items,

which may cause severe danger to the public. And changing shifts frequently will cost a large number of human resources, which is not advisable.

Therefore, a rapid, accurate and automatic approach to assist inspectors to detect prohibited items in X-ray scanned images is desired eagerly. As the technology of deep learning [14] especially the convolutional neural network develops [3, 35], the recognition of occluded prohibited items from X-ray pictures can be regarded as an object detection problem of computer vision, which is widely studied in the literature.

There are several works trying to solve occlusion problems in different scenarios, such as person re-identification [37, 42, 43], face recognition [6, 28, 38]. The object occlusion in Person Re-identification or Face Recognition belongs to intra-class occlusion, and every occluded object has a corresponding annotation. Therefore, a loss function can be designed by annotation information to decrease the impact of occlusion. However, object occlusion in X-ray images for security inspection often exists between prohibited items and safety items, which belongs to inter-class occlusion. For the prohibited items detection task, what we obtained are the annotations of prohibited items, so methods of these senses can not be used for comparison. To the best of our knowledge, up to now, no dataset targeting occluded prohibited items detection in X-ray images has been proposed by researchers even there are also two released X-ray benchmark, namely GDXray [17] and SIXray [18]. However, GDXray [17] contains images which are grayscale, while another dataset SIXray [18] only contains less than 1% images having annotated prohibited items. And both GDXray [17] and SIXray [18] are used for classification task. As a result, both of the two datasets are inconsistent with our task that detecting occluded prohibited items.

To address the above problems, we build up a dataset named Occluded Prohibited Items X-ray (OPIXray) and propose a De-occlusion Attention Module (DOAM) to handle the task of detecting occluded prohibited items in X-ray images. OPIXray contains 8885 labeled X-ray images of 5 categories of cutters (illustrated in Fig. 1), considering that cutter is the most common tool passengers carry. Besides, each of the images has one or more prohibited items. Our dataset is much more challenging and high-quality in two-folds. First, OPIXray mimics a similar testing environment to the real-world scenario, where items randomly overlapped with each other, leading to object occlusion challenge. And five categories of cutters have similar shapes, e.g., folding knives and multi-functional knives, bringing difficulties for machines to distinguish. Second, the prohibited items in these X-ray images are annotated manually by the professional inspectors from an international airport and the standard of annotating is based on the standard of training security inspectors.

Inspired by that security inspectors recognize a prohibited item through focusing on the whole outline and visible partial properties like texture, color, etc. (what we call the region information), the two sub-modules, Edge Information Extraction Module (EIEM) and Region Information Aggregation Module (RIAM), magnify the edge and region information of the prohibited item. DOAM generates an attention distribution map as a high-quality mask for each input image to produce a high-quality feature map, serving identifiable information for detectors.

The main contributions of this work are as follows:

- We provide the first benchmark for occluded prohibited items detection in X-ray images for security inspection. The OPIXray dataset we contributed is high-quality because all prohibited items are manually annotated by professional security inspectors we hired from an international airport.
- We present the De-occlusion Attention Module (DOAM), which integrates two kinds of information that contribute to the detection highly, edge and region information of prohibited items and effectively addresses object occlusion in X-ray images.
- DOAM can be easily inserted as a plug-and-play module into various detectors, including SSD [15], YOLOv3 [23] and FCOS [33], etc., which means our module can be widely applied.
- We evaluate our method on the OPIXray dataset and compare it to several baselines, including popular detection approaches, including SSD [15], YOLOv3 [23], and FCOS [33] and attention mechanisms, including SE [10], Non-local [36] and DA [5]. As is shown from the results, our method achieves better performances.

2 RELATED WORK

2.1 X-ray Images and Benchmarks

The imaging principle of the X-ray images irradiates the objects with X-ray and renders them with pseudo colors according to their spectral absorption rates. As a result, objects made of different materials in X-ray images are assigned with quite different colors, e.g., metals are often shown in blue while impenetrable objects are often shown in red. X-ray offers powerful ability in many tasks such as medical imaging analysis [1, 9, 16] and security inspection [11, 18]. Besides, the object overlapping causes X-ray images differ from natural images highly, because X-ray is often applied in the scenarios that some objects may heavily occlude by others, e.g., personal items are often randomly stacked in a piece of baggage.

Several studies in the literature have attempted to address this challenging problem and designed much work. Unfortunately, due to the particularity of security inspection, very few X-ray datasets have been published for research, and these technologies are severely affected by the occlusion caused by object overlapping. A recently released benchmark, GDXray[17] contains 19407 images, which belongs to three categories of prohibited items including gun, shuriken and razor blade. However, GDXray only contains gray-scale images in a very simple background, as well as clutters and overlaps. As a result, it is easy to recognize or detect the items in the images. SIXray[18] is a large-scale X-ray dataset which is about 100 times larger than the GDXray dataset[17]. SIXray consists of 1059231 X-ray images, but the positive samples are less than 1% to mimic a similar testing environment to the real-world scenario where inspectors often aim at recognizing prohibited items appearing in a very low frequency. Different from ours, SIXray is a dataset for the task of classification, focusing on the problem of data imbalance.

2.2 Attention Mechanism

Attention can be interpreted as a means of biasing the allocation of available computational resources towards the most informative components of a signal, which has been widely studied in many tasks, like image retrieval [30, 40], visual question answering [20, 41]. It captures long-range contextual information and has been widely applied in various tasks such as machine translation [34], image captioning [2], scene segmentation [5] and object recognition [32]. The work [36] is related to self-attention module, mainly exploring the effectiveness of non-local operation in space-time dimensions for videos and images. Jun Fu *et al.* [5] proposed a dual attention network (DANet) for scene segmentation by capturing contextual dependence based on the self-attention mechanism, modeling the semantic interdependencies in spatial and channel dimensions respectively. Squeeze-and-Excitation Networks (SENet) [10] terms the Squeeze-and-Excitation block (SE), that adaptively recalibrates channel-wise feature responses by explicitly modeling interdependencies between channels.

2.3 Object Detection

Object detection is a classical problem in computer vision. With the rise of deep learning, CNN-based methods have become the dominant object detection solution. Most of the methods can be further divided into two general approaches: proposal-free detectors and proposal-based detectors. The first line of work follows a one-stage training strategy and does not explicitly generate proposal boxes, which is pioneered by SSD [15] and YOLO [21–23]. On the other hand, the second line, pioneered by RCNN serials [7, 8, 24], extracts class-agnostic region proposals of the potential objects from a given image. These boxes are then further refined and classified into different categories by a specific module [24, 26, 29, 31]. An advantage of this strategy is that it can filter out many negative locations by the RPN module which facilitates the next detector task. More recently, [4, 12, 13, 33, 39] solved the problem of traditional methods relying heavily on the anchor box, with the only post-processing non-maximum suppression [19]. In this work, we make performance comparisons for our method DOAM with selected approaches from the works above as baselines to show the effectiveness of our approach.

Table 1: The category distribution of the OPIXray dataset. Due to that some images contain more than one prohibited item, the sum of all items in the different categories is greater than the total number of images.

| OPIXray | Categories | | | | | Total |
|----------|------------|----------|---------|---------|------------|-------|
| | Folding | Straight | Scissor | Utility | Multi-tool | |
| Training | 1589 | 809 | 1494 | 1635 | 1612 | 7109 |
| Testing | 404 | 235 | 369 | 343 | 430 | 1776 |
| Total | 1993 | 1044 | 1863 | 1978 | 2042 | 8885 |

3 THE OPIXRAY DATASET

The key to occluded prohibited items detection lies in the memory ability of the pertinent model when presented with prohibited items. Thus, a professional dataset with high-quality annotations is

Table 2: The category distribution of different occlusion levels in the testing set.

| Testing set | Categories | | | | | Total |
|-------------|------------|----------|---------|---------|------------|-------|
| | Folding | Straight | Scissor | Utility | Multi-tool | |
| OL1 | 206 | 88 | 160 | 214 | 255 | 922 |
| OL2 | 148 | 84 | 126 | 88 | 105 | 548 |
| OL3 | 50 | 63 | 83 | 41 | 70 | 306 |
| Total | 404 | 235 | 369 | 343 | 430 | 1776 |

necessary for training models that can detect prohibited items and for performing convincing evaluation as well. We build the first dataset specially designed for occluded prohibited items detection in security inspection.

3.1 Data properties

Data Acquisition: All images of OPIXray dataset are scanned by security inspection machine and annotated manually by professional inspectors from an international airport, and the standard of annotating is based on the standard of training security inspectors. These X-ray images still retain the specific property that different colors are assigned to the objects made of different materials, and every prohibited item is localized by a box-level annotation with a bounding box.

Data Structure: OPIXray dataset contains a total of 8885 X-ray images of 5 categories of cutters, namely, Folding Knife, Straight Knife, Scissor, Utility Knife, Multi-tool Knife. A statistics of category distribution is shown in Tab. 1. All images are stored in JPG format with the resolution of 1225*954. The dataset is partitioned into a training set and a testing set, with the former containing 80% of the images (7109) and the latter containing 20% (1776), where the ratio is about 4 : 1. The statistics of category distribution of training set and testing set are also shown in Tab. 1.

Data Occlusion Levels: In order to study the impact brought by object occlusion levels, we divide the testing set into three subsets and name them Occlusion Level 1 (OL1), Occlusion Level 2 (OL2) and Occlusion Level 3 (OL3), where the number indicates occlusion level of prohibited items in images. There is no or slight occlusion on prohibited items in OL1 and partial occlusion in OL2. To maximally evaluate the ability of models to deal with object occlusion, we construct OL3 by choosing images where severe or full occlusions exists. The category distribution of the three subsets with different occlusion levels are shown in Tab. 2.

3.2 Dataset Analysis

Data Authenticity: OPIXray dataset mostly mimics a similar environment to the real-world scenario. **First**, the occlusion of prohibited items is inspired that items within personal luggage are usually stacked randomly and overlapped with each other, which we describe detailedly in this work. **Second**, the statics of category distribution is inconsistent obviously. The number of folding knife and multi-tool knife are higher than straight knife because the former two categories are more common for passengers to bring. And the number of OL3 is significantly less than OL1 because cutters are seldom fully occluded in the real scenario.

Data Application: OPIXray dataset has two major application scenarios. **First**, the dataset can evaluate the ability of a model to detect prohibited items in X-ray images. A better model can achieve better performance no matter which occluded levels. As we can see from Fig. 3, there is a significant decline in the performance of famous detection approaches e.g., SSD [15] and YOLOv3 [23], with the occlusion level increasing. **Second**, the dataset can evaluate the ability of a model to solving object occlusion problem, by comparing the improvement amount than other methods in different occlusion level settings. The improvement amount of an approach increases with the occlusion level increases, which illustrates the effectiveness of the approach to the object occlusion problems.

4 DE-OCCULTATION ATTENTION MODULE

We propose a De-occlusion Attention Module (DOAM) to magnify considerable information, which can serve a refined feature map to help the detector to recognize more easily. Central to DOAM are Edge Information Extraction Module (EIEM) and Region Information Aggregation Module (RIAM) that capturing edge information and the region information of the prohibited item respectively, and Hybrid Attention Generation (HAG) generating the attention

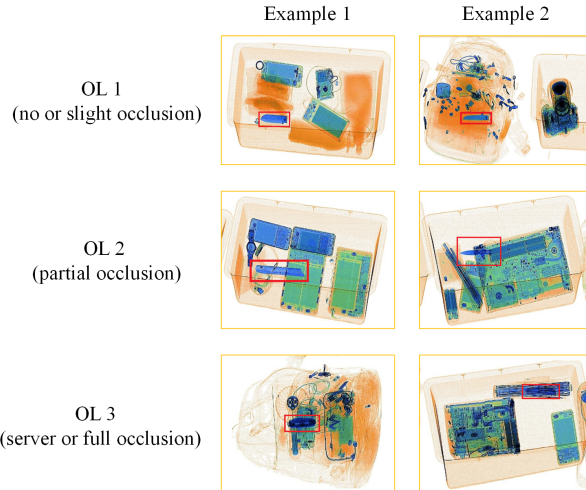


Figure 2: Samples of different occlusion levels.

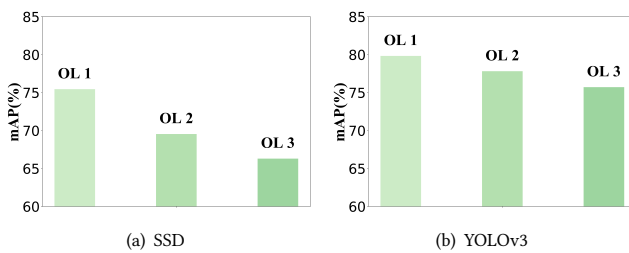


Figure 3: The performance of SSD [15] and YOLOv3 [23] under three different object occlusion levels.

map by hybridizing the two feature maps generated by EIEM and RIAM. Next, we first present the general framework of DOAM, and describe EIEM and RIAM respectively. We further introduce the hybrid process of HAG and finally analyze the complexity and attention intensity of DOAM.

4.1 The General Framework of DOAM

As illustrated in Fig. 4, given an x-ray image, simulating the real-world scenario, in which objects in the luggage are placed randomly, including prohibited items we desire to detect. We employ a pre-trained network with the dilated strategy as the backbone. The input image is fed into EIEM and RIAM to generate two feature maps, F_E and F_R , utilizing edge and region information of prohibited items respectively.

In EIEM, we extract the edge image from the input image by the edge detection operation and optimize the particular loss function so as to generate the feature map F_E which emphasizes edge information of prohibited items. F_E retains complete edge information of the prohibited item in the input image, which likes that security inspectors see the outline of the object.

In RIAM, we concatenate the input image and the corresponding edge image and extract a temporary feature map F_{tmp1} from the concatenated image. Further, we draw the Region Information Aggregation (RIA) operation, which is central to RIAM, to refine F_{tmp1} and generate a refined feature map F_R . F_R emphasizes region information of prohibited items is generated, remaining information of identifiable properties of the visible part of prohibited items.

We fuse the two feature maps F_E and F_R to generate an attention map, and finally utilize the attention map to generate a refined feature map. The entire process of DOAM is detailed in Algorithm 1.

4.2 Edge Information Extraction Module (EIEM)

Suppose there are n training images in the dataset $X = \{x_1, \dots, x_n\}$. For each input image $x \in X$, we utilize the convolutional neural network with the horizontal and vertical kernel denoted as s_h, s_v of the Sobel operator, to respectively compute the edge images E^h and E^v for the horizontal and vertical directions. We further generate the edge image E of the input image x by synthesizing the above two results E^h and E^v . To lead EIEM to only magnify edge information of the prohibited items, we use N_1 network blocks (Here, we define N_1 as the Module Operation Intensity of EIEM, which represents that the performance of the module changes with the value of N_1 . And the proper value of N_1 will be discussed later), in which each block consists of a convolutional layer with a 3×3 kernel size, a batch normalization layer, and a relu layer, to extract the feature map F_E of the edge image E . The operations can be formulated as follows:

$$f_e(x) = \text{relu}(\mathbf{W}_e \cdot x + \mathbf{b}_e). \quad (1)$$

$$\mathbf{F}_E = \{f_e(\mathbf{E})\}_{N_1}. \quad (2)$$

where $\{\cdot\}_{N_1}$ means that the operation is repeated N_1 times, $\mathbf{W}_e, \mathbf{b}_e$ are parameters of the convolutional layer. After extracting the feature map F_E as shown in Eq. 2 above, we adaptively attend to

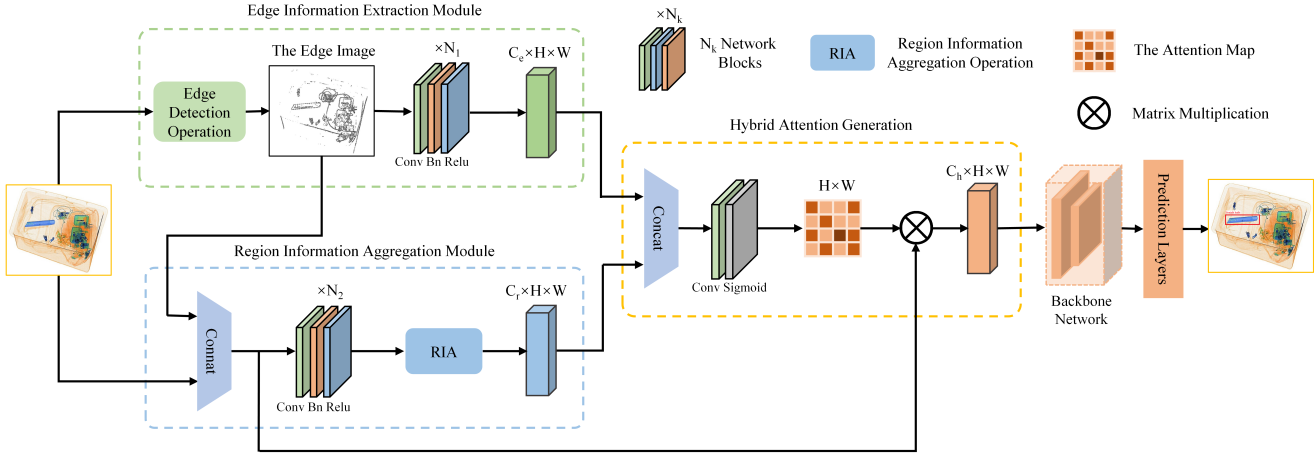


Figure 4: DOAM integrated with a general backbone network architecture. As illustrated, two feature maps generated by Edge Information Extraction Module (EIEM) and Region Information Aggregation Module (RIAM) and hybridized in Hybrid Attention Generation (HAG). Further, DOAM generates an attention map and applies the attention map to the input image to generate the refined feature map we desire. Finally, the refined feature map can be utilized by any architectures integrated.

Algorithm 1 The Operation Process of DOAM.

- 1: **Input:** an X-ray image $\mathbf{x} \in \mathbb{R}^{C \times H \times W}$;
- 2: Generate the horizontal edge image \mathbf{E}^h and the vertical edge image \mathbf{E}^v by the Sobel operator.
- 3: Generate the edge image \mathbf{E} by synthesizing \mathbf{E}^h and \mathbf{E}^v .
- 4: **for** N_1 steps **do**
- 5: Refine the feature map \mathbf{F}_E by operating \mathbf{E} through $f_E(\cdot)$.
- 6: **end for**
- 7: Generate the concatenated image \mathbf{P} by concatenating \mathbf{x} and \mathbf{E} .
- 8: **for** N_2 steps **do**
- 9: Refine the feature map \mathbf{F}_{tmp1} by operating \mathbf{P} through $f_r(\cdot)$.
- 10: **end for**
- 11: **for** $k \in \{k_1, \dots, k_n\}$ **do**
- 12: Generate refined feature map \mathbf{F}_{tmp2}^k by operating \mathbf{F}_{tmp1} through Eq. (6).
- 13: Generate refined feature map \mathbf{F}_{tmp3}^k by concatenating \mathbf{F}_{tmp1} and \mathbf{F}_{tmp2}^k .
- 14: Update the feature map set $S = S \cup \mathbf{F}_{tmp3}^k$.
- 15: **end for**
- 16: Choose the appropriate feature map \mathbf{F}_R from S by drawing the gated convolutional network.
- 17: Generate the fused feature map \mathbf{F}_{fus} by operating \mathbf{F}_E and \mathbf{F}_R .
- 18: Generate the attention map $\mathbf{M} = \sigma(\mathbf{F}_{fus})$.
- 19: Generate the final feature map \mathbf{F} by performing a matrix multiplication between \mathbf{M} and \mathbf{P} .
- 20: **Output:** the refined feature map $\mathbf{F} \in \mathbb{R}^{C_h \times H \times W}$.

the edge information of the prohibited item within the feature map \mathbf{F}_E by optimizing a specific loss function.

4.3 Region Information Aggregation Module (RIAM)

For every point of the feature map, in order to construct relations between each position and a certain region around it, we utilize N_2 network blocks (As we state in EIEM, N_2 is the Module Operation Intensity of RIAM and the value of N_2 will be discussed later), in which each block consists a convolutional layer with the kernel size is 3×3 , a batch normalization layer, a relu layer, to extract a temporary feature map \mathbf{F}_{tmp1} from the concatenated image (concatenating the input image \mathbf{x} with its corresponding edge image \mathbf{E}) as follows:

$$\mathbf{P} = \mathbf{x} \parallel \mathbf{E}. \quad (3)$$

$$f_r(\mathbf{x}) = \text{relu}(\mathbf{W}_r \cdot \mathbf{x} + \mathbf{b}_r). \quad (4)$$

$$\mathbf{F}_{tmp1} = \{f_r(\mathbf{P})\}_{N_2}. \quad (5)$$

where \parallel represents concatenating operation. We further generate the refined feature map \mathbf{F}_R of RIAM by refining \mathbf{F}_{tmp1} through the Region Information Aggregation (RIA) operation, central of RIAM.

Fig. 5 illustrates the detailed process of RIA operation. For the input feature map \mathbf{F}_{tmp1} and a parameter k , RIA operation aggregates the information of a certain size of $k \times k$ of region around it by average pooling and extending to generate another temperate feature map \mathbf{F}_{tmp2}^k . The average pooling and extending operations can be formulated together as follows:

$$\mathbf{F}_{tmp2}^k_{ij} = \frac{\sum_{m=i-(i \bmod k)}^{i-(i \bmod k)+k} \sum_{n=j-(j \bmod k)}^{j-(j \bmod k)+k} \mathbf{F}_{tmp1}^{mn}}{k^2}. \quad (6)$$

where $\mathbf{F}_{tmp2}^k_{ij}$ represents the feature of the i -th row and j -th column of feature map \mathbf{F}_{tmp2} when the kernel size for the average pooling layer is k .

We further concatenate the two feature maps (\mathbf{F}_{tmp1} and \mathbf{F}_{tmp2}^k) in the dimension of channel to generate a new feature map \mathbf{F}_{tmp3}^k , where the dimensions are $2C_r \times H \times W$. Then every point of the new

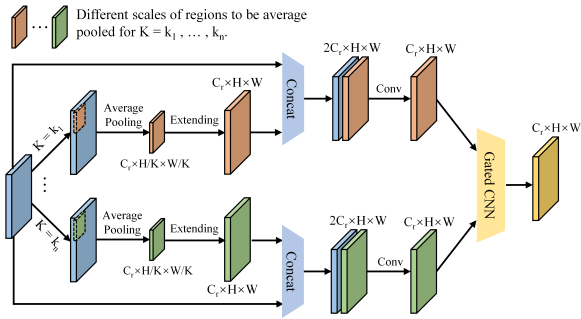


Figure 5: The Operation Process of RIA.

feature map has the ability to perceive the region of size $k \times k$ around it, which means that the relations have been constructed. Due to different sizes of region information to aggregate (different values of k), the module generates a feature map set $S = \{F_{tmp3}^{k_1}, \dots, F_{tmp3}^{k_n}\}$.

In order to enable RIA operation to perform well on various scales of prohibited items, it is necessary to design a mechanism to adaptively choose an optimal value for k . We exploit the gated convolutional neural network [?] \mathbb{G} with 3×3 kernels into RIA, to select the proper feature map F_R from the feature map set S as output. The operations are formulated as follows:

$$F_R = \mathbb{G}(S). \quad (7)$$

where $S = \{F_{tmp3}^{k_1}, \dots, F_{tmp3}^{k_n}\}$.

4.4 Hybrid Attention Generation

As is illustrated in Algorithm 1, for the result feature maps F_E and F_R outputted by the EIEM and the RIAM respectively, where $F_E \in \mathbb{R}^{C_e \times H \times W}$, $F_R \in \mathbb{R}^{C_r \times H \times W}$, we concatenate them for information fusion. And further we feed the concatenated feature into a convolutional layer, where the kernel size is 1×1 , to generate the feature map $F_{fus} \in \mathbb{R}^{(C_e + C_r) \times H \times W}$, which have confused the edge information and the regional information, both strengthened. The operation can be formulated as follows:

$$F_{fus} = \mathbf{W}_m (F_E || F_R) + \mathbf{b}_m. \quad (8)$$

where $||$ represents the operation of concatenating, and \mathbf{W}_m , \mathbf{b}_m are parameters of the convolutional layer. Then we utilize the feature map F_{fus} as the input of a sigmoid function to generate the attention map M as follows:

$$M = \sigma(F_{fus}) = \frac{1}{1 + e^{-F_{fus}}}. \quad (9)$$

where $M \in \mathbb{R}^{H \times W}$. Finally, we calculate the inner product of the attention map M and the concatenated image P as follows:

$$F_j = \sum_{i=1}^{H \times W} M_{ji} P_i. \quad (10)$$

where $F \in \mathbb{R}^{C_h \times H \times W}$, and it is the final feature map we desire to serve to the detector, of which the information highly contributes to the detection of the prohibited item are magnified.

4.5 Analysis and Discussion

In this section, we first analyze the model complexity with or without DOAM in SSD network [15], and compare the complexity including the total number of parameters, model size and computation cost, with other attention mechanisms. Then, we discuss the performance of our module caused by different values of the two Module Operation Intensities for EIEM and RIAM.

Module Complexity Analysis: Table 3 reports that DOAM only brings a slight increase in computational cost (7.14% in GFLOPs), compared to the SSD [15] without any attention mechanisms. Additionally, we compare the complexity between DOAM and three variants of attention mechanisms, including SE [10], Non-local [36] and DA [5]. The three attention mechanisms focus on channel information, spatial information and combination of the two kinds of information, respectively. As we can see from table 3, compared to the single SSD [15], **First**, for total number of parameters, SE [10], Non-local [36] and DA [5] respectively bring 32.23%, 27.69% and 88.43% increases, while the increase our module brings is almost negligible. **Second**, for model size, SE [10], Non-local [36] and DA [5] respectively bring 31.86%, 27.32% and 88.01% increases, while the increase our module brings is almost negligible. However, for computational cost, SE [10], Non-local [36] and DA [5] respectively bring 3.15%, 6.54% and 23.07% increases, while our module brings 7.14%.

In conclusion, for total number of parameters and model size, DOAM is much more computation efficient than the three famous attention mechanisms. For computational cost, DOAM is slightly more computationally expensive. We conjecture that it is mainly because that the parameter k causes repetitive computation in RIA.

Table 3: Complexity comparison of different models. PARAMs, SIZE and GFLOPs represent the total number of parameters, the Model Size and the Giga Floating Point operations, respectively.

| Method | PARAMs | SIZE(MB) | GFLOPs |
|-----------------------|--------------------|-------------|----------------|
| SSD [15] | 24.2×10^6 | 92.6 | 30.6522 |
| SSD+SE [10] | 32.0×10^6 | 122.1 | 31.6169 |
| SSD+Non-local [36] | 30.9×10^6 | 117.9 | 32.6577 |
| SSD+DA [5] | 45.6×10^6 | 174.1 | 37.7231 |
| SSD+DOAM(ours) | 24.3×10^6 | 92.7 | 32.8435 |

Module Operation Intensity Discussion: The value of Module Operation Intensity means the number of convolutional layers of an attention module network. Experience tells us, the performance of a network improves with the number of convolutional layer increases. However, as we can see from Fig. 6, it is not like that in DOAM. Therefore, choosing appropriate values of the two Module Operation Intensities, N_1 of EIEM and N_2 of RIAM can not only improve the performance, but also effectively reduce the complexity and improve the executive efficiency of DOAM.

Fig. 6 shows that the two values of N_1 and N_2 have an obvious impact on the performance of the model. When both of the two numbers are 5, DOAM achieves the best performance. Usually that the performance of a model increases with the number of the convolution layers, which mainly applicable to the case with enough

data. However, when the data is hungry, complex network causes the overfitting easily, leading to the poor generalization ability of the model. We construct the network structure according to the experiment of parameter comparison, which highly matches the OPIXray dataset.

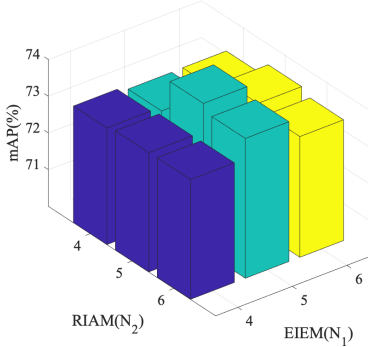


Figure 6: Performance comparison of DOAM with different values of the attention intensities of EIEM and RIAM.

Table 4: Performance comparison between DOAM and other different attention mechanisms on object categories. FO, ST, SC, UT and MU represent Folding Knife, Straight Knife, Scissor, Utility Knife and Multi-tool Knife, respectively.

| Method | mAP | Categories | | | | |
|-----------------------|--------------|--------------|--------------|--------------|--------------|--------------|
| | | FO | ST | SC | UT | MU |
| SSD [15] | 70.89 | 76.91 | 35.02 | 93.41 | 65.87 | 83.27 |
| SSD+SE [10] | 71.85 | 77.17 | 38.29 | 92.03 | 66.10 | 85.67 |
| SSD+Non-local [36] | 71.41 | 77.55 | 36.38 | 95.26 | 64.86 | 82.98 |
| SSD+DA [5] | 71.96 | 79.68 | 37.69 | 93.38 | 64.14 | 84.90 |
| SSD+DOAM(ours) | 74.01 | 81.37 | 41.50 | 95.12 | 68.21 | 83.83 |

5 EXPERIMENTS

In this section, we carry on extensive experiments to evaluate the DOAM we proposed. **First**, we verify that DOAM outperforms all the attention mechanisms mentioned above, over different categories and different occlusion levels. **Second**, we perform ablation experiments to thoroughly evaluate the effectiveness of DOAM. **Third**, we demonstrate the general applicability of DOAM across different architectures and the effectiveness after DOAM-integrated. **Finally**, we apply the Grad-CAM [25] to visualize the attention mechanism of DOAM.

Evaluation strategy: All experiments are carried on the OPIXray dataset. In experiments of comparing with different attention mechanisms over different occlusion levels, every model is trained by training set data in Tab. 1 and tested on OL1, OL2 and OL3 5 respectively. In any other experiment, every model is trained by training set data and tested by the testing set data in Tab. 1.

Baseline Detail: In experiments of comparing with different attention mechanisms, we respectively plug DOAM and each of the

attention modules into SSD [15] and report the performances of SSD [15] and these integrated networks. In ablation study, we plug each sub-module of DOAM into SSD [15] separately and report the performances of SSD [15] and these integrated networks. In experiments of comparing with different detection approaches, we plug DOAM into a number of popular detection networks and report the model performance with or without DOAM in every detection network.

Parameter setting: In all experiments following, all models are optimized by the SGD optimizer and the learning rate is set to 0.0001. The batch size is set to 24 and the momentum and weight decay are set to 0.9 and 0.0005 respectively. We evaluate the mean Average Precision (mAP) of the object detection to measure the performance of the model and the IOU threshold is set to 0.5. We further select the best performance model to calculate the AP of each category to observe the performance improvement in different categories. Furthermore, in order to avoid the influence of image data modification on edge image generation, we do not use any data augmentation methods to expand the data or modify the pixel value of the original image, which helps us to better analyze the impact of edge information.

5.1 Comparing with Different Attention Mechanisms

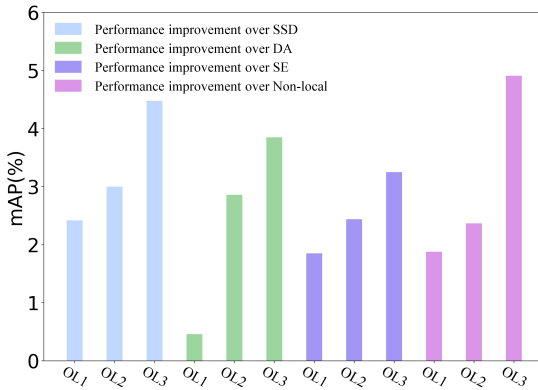
We compare three variants of attention mechanisms above, including SE [10], Non-local [36] and DA [5]. Tab. 4 and 5 reports the performances of all models.

Object Categories: As we can observe from Tab. 4, the DOAM-integrated model outperforms SSD [15] by 3.12%. Besides, DOAM outperforms SE [10], Non-local [36] and DA [5], by 2.16%, 2.60%, 2.05%, respectively. Moreover, Tab. 4 shows the improvement of DOAM is mainly reflected in Straight Knife, Folding Knife and Utility Knife, all of which are with the high level occlusion. Especially for Straight Knife, which is the category with highest level occlusion, DOAM outperforms SSD [15] by an impressive amount of 6.48% and Non-local [36] by 5.12%. For Scissor, the lightest occlusion category, the performance of DOAM is only improved by 1.71% compared to SSD [15] and similar to Non-local [36]. It is obvious that DOAM surpasses these current popular attention mechanisms over different categories.

Object Occlusion Levels: The experimental results are shown in Tab. 5. Further, Fig. 7 is drawn according to Tab. 5 to illustrate the effectiveness of DOAM to occluded object detection in X-ray images more clearly. In Fig. 7, we can clearly obtain a conclusion that DOAM can achieve a higher performance than the baseline and other attention mechanisms with the X-ray images suffer a higher level of occlusion. It verifies the effectiveness of DOAM that it has a significant effect on the performance of detecting occluded prohibited items in X-ray images. (Note that in OL3, the performance of "SSD+Non-local" is lower than "SSD". Due to the attention mechanism of Non-local is to capture spatial information by constructing the relations between regions, we conjecture that this type of relation reduces effect when the noises of image increase.)

Table 5: Performance comparison between DOAM and other different attention mechanisms on object occlusion levels.

| Method | OL 1 | OL 2 | OL 3 |
|-----------------------|--------------|--------------|--------------|
| SSD [15] | 75.45 | 69.54 | 66.30 |
| SSD+SE [10] | 76.02 | 70.11 | 67.53 |
| SSD+Non-local [36] | 75.99 | 70.17 | 65.87 |
| SSD+DA [5] | 77.41 | 69.68 | 66.93 |
| SSD+DOAM(ours) | 77.87 | 72.45 | 70.78 |

**Figure 7: The amount changes of performance improvement of DOAM over different models with occlusion level increasing.**

5.2 Ablation Study

Tab. 6 shows that EIEM improved the performance by 0.43% compared with the method of simply concatenating the input image and the corresponding edge image without any other operations of EIEM. We conjecture that it is mainly because the EIEM has the ability to focus adaptively on the prohibited items we desire to detect by specifically increasing the weight of edge information through the optimization of a loss function, while simply concatenating operates all the objects in the image equally whether the object is we desire to detect or not for feature fusion.

Besides, model integrating both EIEM and RIAM achieves better performance by 0.37% than integrating EIEM alone, which verifies the effectiveness of RIAM. Note that we observe prohibited item size is about 10×10 averagely, so we choose 10×10 as the region scale to perceive for each position of the feature map.

We choose three different scales of the regions (5×5 , 10×10 , 15×15 respectively), and draw the gated convolutional neural network [?] \mathbb{G} into RIAM, to adaptively select the best feature map which generated by operation of average pooling with appropriate pooling size. The experimental results show that after drawing \mathbb{G} , the performance improves by 0.9%.

Table 6: Ablation studies of DOAM. C represents simply concatenate operation, E represents Edge Information Extraction Module, R represents Region Information Aggregation Module, and \mathbb{G} represents drawing the Gate Convolutional Neural Network [?].

| Method | mAP | Category | | | | |
|--------------------------------|--------------|--------------|--------------|--------------|--------------|--------------|
| | | FO | ST | SC | UT | MU |
| SSD [15] | 70.89 | 76.91 | 35.02 | 93.41 | 65.87 | 83.27 |
| SSD+C | 72.32 | 79.00 | 36.46 | 94.13 | 68.85 | 83.18 |
| SSD+E | 72.75 | 80.26 | 35.54 | 94.81 | 67.96 | 85.19 |
| SSD+E+R(without \mathbb{G}) | 73.12 | 79.94 | 38.58 | 93.39 | 69.40 | 84.28 |
| SSD+DOAM(E+R) | 74.01 | 81.37 | 41.50 | 95.12 | 68.21 | 83.83 |

5.3 Comparing with Different Detection Approaches

To further evaluate the effectiveness of DOAM and verify DOAM can be applied to various detection networks, we conduct experiments on the famous detection approaches, SSD [15], YOLOv3 [23] and FCOS [33]. The results are shown in Tab. 7.

Table 7: Performance comparison between DOAM-integrated network and baselines for three famous detection approaches.

| Method | mAP | Category | | | | |
|--------------------------|--------------|--------------|--------------|--------------|--------------|--------------|
| | | FO | ST | SC | UT | MU |
| SSD [15] | 70.89 | 76.91 | 35.02 | 93.41 | 65.87 | 83.27 |
| SSD+DOAM(ours) | 74.01 | 81.37 | 41.50 | 95.12 | 68.21 | 83.83 |
| YOLOv3 [23] | 78.21 | 92.53 | 36.02 | 97.34 | 70.81 | 94.37 |
| YOLOv3+DOAM(ours) | 79.25 | 90.23 | 41.73 | 96.96 | 72.12 | 95.23 |
| FCOS [33] | 82.02 | 86.41 | 68.47 | 90.22 | 78.39 | 86.60 |
| FCOS+DOAM(ours) | 82.41 | 86.71 | 68.58 | 90.23 | 78.84 | 87.67 |

As we can see from Tab. 7, the performance of DOAM-integrated networks are improved by 3.12%, 1.04% and 0.39% compared with SSD [15], YOLOv3 [23] and FCOS [33] respectively, which verify that our module can be inserted as a plug-and-play module into most detection networks and receive a better performance. Note that the performances on Folding Knife and Scissor after DOAM-integrated are slightly reduced. We speculate that the reason is that these images of the two categories in the dataset are occluded not seriously. When the occlusion level increases, the attention mechanism pays more attention to the objects occluded highly like straight knives while less attention to the objects occluded slightly, which results in the slight performance degradation for Folding Knife and Scissor.

5.4 Attention Visualization Analysis

The effects of DOAM can be visualized in Fig. 8. In rows 1 and 3, we select 10 input X-ray images (each category has two images) and show their corresponding attention visualizations in rows 2 and 4. We observe that DOAM could capture edge and region information accurately. For example, in column 4, a red box is marked on a

utility knife of the X-ray image (in row 1), and the boundaries of the utility knife are very clear in the attention visualization (in row 2). Moreover, in the first column, a red box is marked on a folding knife and the corresponding attention map (in row 2) highlights most the areas where the folding knife lies on. In short, these visualizations further demonstrate the effectiveness of capturing edge and region information for improving feature representation in occluded prohibited items detection.

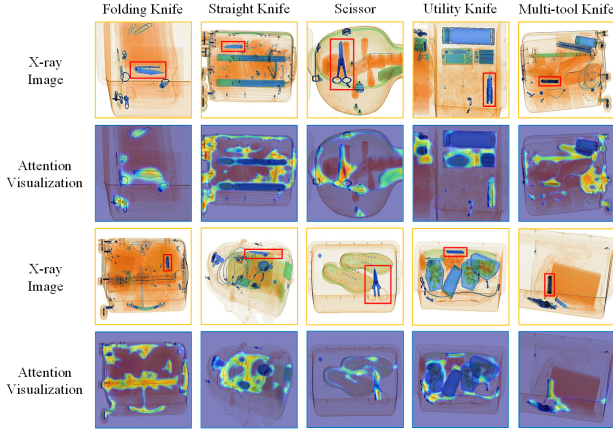


Figure 8: Attention visualization results.

6 CONCLUSION

In this paper, we investigate occluded prohibited items detection in X-ray scanned images, which is a promising application in industry yet remains fewer studied in computer vision. To facilitate research in this field, we present a first high-quality dataset OPIXray, mainly focusing on occlusion of the objects in the images. All the backgrounds of which were captured from the real-world scenarios and the prohibited items are annotated manually by the professional inspectors from an international airport and the standard of annotating is based on the standard of training security inspectors.

Motivated by filtering irrelevant information of attention mechanisms, we present an attention module named DOAM, which can be applied to various popular detection approaches, to refine the features to the detectors. In practice, we design two sub-modules, EIEM and RIAM, extracting the information of interest respectively. As shown in experiments, DOAM surpasses the popular attention mechanisms and the DOAM-integrated network surpasses popular detection approaches obviously. The data and code link is <https://github.com/OPIXray-author/OPIXray>.

REFERENCES

- [1] Arjun Chaudhary, Abhishek Hazra, and Prakash Chaudhary. 2019. Diagnosis of Chest Diseases in X-Ray images using Deep Convolutional Neural Network. In *2019 10th International Conference on Computing, Communication and Networking Technologies (ICCCNT)*. IEEE, 1–6.
- [2] Long Chen, Hanwang Zhang, Jun Xiao, Liqiang Nie, Jian Shao, Wei Liu, and Tat-Seng Chua. 2017. Sca-cnn: Spatial and channel-wise attention in convolutional networks for image captioning. In *Proceedings of the IEEE conference on computer vision and pattern recognition*. 5659–5667.
- [3] Zhi-Qi Cheng, Jun-Xiu Li, Qi Dai, Xiaowu, Jun-Yan He, and Alexander G Hauptmann. 2019. Improving the learning of multi-column convolutional neural network for crowd counting. In *Proceedings of the 27th ACM International Conference on Multimedia*. 1897–1906.
- [4] Kaiwen Duan, Song Bai, Lingxi Xie, Honggang Qi, Qingming Huang, and Qi Tian. 2019. Centernet: Keypoint triplets for object detection. In *Proceedings of the IEEE International Conference on Computer Vision*. 6569–6578.
- [5] Jun Fu, Jing Liu, Haijie Tian, Yong Li, Yongjun Bao, Zhiwei Fang, and Hanqing Lu. 2019. Dual attention network for scene segmentation. In *Proceedings of the IEEE Conference on Computer Vision and Pattern Recognition*. 3146–3154.
- [6] Shiming Ge, Jia Li, Qiting Ye, and Zhao Luo. 2017. Detecting masked faces in the wild with lle-cnn. In *Proceedings of the IEEE Conference on Computer Vision and Pattern Recognition*. 2682–2690.
- [7] Ross Girshick. 2015. Fast r-cnn. In *Proceedings of the IEEE international conference on computer vision*. 1440–1448.
- [8] Ross Girshick, Jeff Donahue, Trevor Darrell, and Jitendra Malik. 2014. Rich feature hierarchies for accurate object detection and semantic segmentation. In *Proceedings of the IEEE conference on computer vision and pattern recognition*. 580–587.
- [9] Shuai Guo, Songyuan Tang, Jianjun Zhu, Jingfan Fan, Danni Ai, Hong Song, Ping Liang, and Jian Yang. 2019. Improved U-Net for Guidewire Tip Segmentation in X-ray Fluoroscopy Images. In *Proceedings of the 2019 3rd International Conference on Advances in Image Processing*. 55–59.
- [10] Jie Hu, Li Shen, and Gang Sun. 2018. Squeeze-and-excitation networks. In *Proceedings of the IEEE conference on computer vision and pattern recognition*. 7132–7141.
- [11] Shengling Huang, Xin Wang, Yifan Chen, Jie Xu, Tian Tang, and Baozhong Mu. 2019. Modeling and quantitative analysis of X-ray transmission and backscatter imaging aimed at security inspection. *Optics express* 27, 2 (2019), 337–349.
- [12] Hei Law and Jia Deng. 2018. Cornernet: Detecting objects as paired keypoints. In *Proceedings of the European Conference on Computer Vision (ECCV)*. 734–750.
- [13] Hei Law, Yun Teng, Olga Russakovsky, and Jia Deng. 2019. Cornernet-lite: Efficient keypoint based object detection. *arXiv preprint arXiv:1904.08900* (2019).
- [14] Yann LeCun, Yoshua Bengio, and Geoffrey Hinton. 2015. Deep learning. *nature* 521, 7553 (2015), 436–444.
- [15] Wei Liu, Dragomir Anguelov, Dumitru Erhan, Christian Szegedy, Scott Reed, Cheng-Yang Fu, and Alexander C Berg. 2016. Ssd: Single shot multibox detector. In *European conference on computer vision*. Springer, 21–37.
- [16] Jianjie Lu and Kai-yu Tong. 2019. Towards to Reasonable Decision Basis in Automatic Bone X-Ray Image Classification: A Weakly-Supervised Approach. In *Proceedings of the AAAI Conference on Artificial Intelligence*, Vol. 33. 9985–9986.
- [17] Domingo Mery, Vladimir Riffo, Uwe Zscherpel, German Mondragón, Iván Lillo, Irene Zuccar, Hans Lobel, and Miguel Carrasco. 2015. GDXray: The database of X-ray images for nondestructive testing. *Journal of Nondestructive Evaluation* 34, 4 (2015), 42.
- [18] Caijing Miao, Lingxi Xie, Fang Wan, Chi Su, Hongye Liu, Jianbin Jiao, and Qixiang Ye. 2019. Sixray: A large-scale security inspection x-ray benchmark for prohibited item discovery in overlapping images. In *Proceedings of the IEEE Conference on Computer Vision and Pattern Recognition*. 2119–2128.
- [19] Alexander Neubek and Luc Van Gool. 2006. Efficient non-maximum suppression. In *18th International Conference on Pattern Recognition (ICPR'06)*, Vol. 3. IEEE, 850–855.
- [20] Liang Peng, Yang Yang, Zheng Wang, Xiao Wu, and Zi Huang. 2019. CRA-Net: Composed Relation Attention Network for Visual Question Answering. In *Proceedings of the 27th ACM International Conference on Multimedia*. 1202–1210.
- [21] Joseph Redmon, Santosh Divvala, Ross Girshick, and Ali Farhadi. 2016. You only look once: Unified, real-time object detection. In *Proceedings of the IEEE conference on computer vision and pattern recognition*. 779–788.
- [22] Joseph Redmon and Ali Farhadi. 2017. YOLO9000: better, faster, stronger. In *Proceedings of the IEEE conference on computer vision and pattern recognition*. 7263–7271.
- [23] Joseph Redmon and Ali Farhadi. 2018. Yolov3: An incremental improvement. *arXiv preprint arXiv:1804.02767* (2018).
- [24] Shaoqing Ren, Kaiming He, Ross Girshick, and Jian Sun. 2015. Faster r-cnn: Towards real-time object detection with region proposal networks. In *Advances in neural information processing systems*. 91–99.
- [25] Ramprasaath R Selvaraju, Michael Cogswell, Abhishek Das, Ramakrishna Vedantam, Devi Parikh, and Dhruv Batra. 2017. Grad-cam: Visual explanations from

deep networks via gradient-based localization. In *Proceedings of the IEEE international conference on computer vision*. 618–626.

[26] Abhinav Shrivastava, Rahul Sukthankar, Jitendra Malik, and Abhinav Gupta. 2016. Beyond skip connections: Top-down modulation for object detection. *arXiv preprint arXiv:1612.06851* (2016).

[27] Karen Simonyan and Andrew Zisserman. 2014. Very deep convolutional networks for large-scale image recognition. *arXiv preprint arXiv:1409.1556* (2014).

[28] Lingxue Song, Dihong Gong, Zhifeng Li, Changsong Liu, and Wei Liu. 2019. Occlusion Robust Face Recognition Based on Mask Learning With Pairwise Differential Siamese Network. In *Proceedings of the IEEE International Conference on Computer Vision*. 773–782.

[29] Ke Sun, Bin Xiao, Dong Liu, and Jingdong Wang. 2019. Deep high-resolution representation learning for human pose estimation. In *Proceedings of the IEEE Conference on Computer Vision and Pattern Recognition*. 5693–5703.

[30] Xie Sun, Lu Jin, and Zechao Li. 2019. Attention-Aware Feature Pyramid Ordinal Hashing for Image Retrieval. In *Proceedings of the ACM Multimedia Asia on ZZZ*. 1–6.

[31] Christian Szegedy, Sergey Ioffe, Vincent Vanhoucke, and Alexander A Alemi. 2017. Inception-v4, inception-resnet and the impact of residual connections on learning. In *Thirty-first AAAI conference on artificial intelligence*.

[32] Jinhui Tang, Lu Jin, Zechao Li, and Shenghua Gao. 2015. RGB-D object recognition via incorporating latent data structure and prior knowledge. *IEEE Transactions on Multimedia* 17, 11 (2015), 1899–1908.

[33] Zhi Tian, Chunhua Shen, Hao Chen, and Tong He. 2019. Fcos: Fully convolutional one-stage object detection. In *Proceedings of the IEEE International Conference on Computer Vision*. 9627–9636.

[34] Ashish Vaswani, Noam Shazeer, Niki Parmar, Jakob Uszkoreit, Llion Jones, Aidan N Gomez, Łukasz Kaiser, and Illia Polosukhin. 2017. Attention is all you need. In *Advances in neural information processing systems*. 5998–6008.

[35] Pichao Wang, Zhaoyang Li, Yonghong Hou, and Wanqing Li. 2016. Action recognition based on joint trajectory maps using convolutional neural networks. In *Proceedings of the 24th ACM international conference on Multimedia*. 102–106.

[36] Xiaolong Wang, Ross Girshick, Abhinav Gupta, and Kaiming He. 2018. Non-local neural networks. In *Proceedings of the IEEE conference on computer vision and pattern recognition*. 7794–7803.

[37] Xinlong Wang, Tete Xiao, Yuning Jiang, Shuai Shao, Jian Sun, and Chunhua Shen. 2018. Repulsion loss: Detecting pedestrians in a crowd. In *Proceedings of the IEEE Conference on Computer Vision and Pattern Recognition*. 7774–7783.

[38] Jian Yang, Lei Luo, Jianjun Qian, Ying Tai, Fanlong Zhang, and Yong Xu. 2016. Nuclear norm based matrix regression with applications to face recognition with occlusion and illumination changes. *IEEE transactions on pattern analysis and machine intelligence* 39, 1 (2016), 156–171.

[39] Ze Yang, Shaohui Liu, Han Hu, Liwei Wang, and Stephen Lin. 2019. Reppoints: Point set representation for object detection. In *Proceedings of the IEEE International Conference on Computer Vision*. 9657–9666.

[40] Xingxu Yao, Dongyu She, Sicheng Zhao, Jie Liang, Yu-Kun Lai, and Jufeng Yang. 2019. Attention-aware polarity sensitive embedding for affective image retrieval. In *Proceedings of the IEEE International Conference on Computer Vision*. 1140–1150.

[41] Zheng-Jun Zha, Jiawei Liu, Tianhao Yang, and Yongdong Zhang. 2019. Spatiotemporal-Textual Co-Attention Network for Video Question Answering. *ACM Transactions on Multimedia Computing, Communications, and Applications (TOMM)* 15, 2s (2019), 1–18.

[42] Shifeng Zhang, Longyin Wen, Xiao Bian, Zhen Lei, and Stan Z Li. 2018. Occlusion-aware R-CNN: detecting pedestrians in a crowd. In *Proceedings of the European Conference on Computer Vision (ECCV)*. 637–653.

[43] Chunluan Zhou and Junsong Yuan. 2018. Bi-box regression for pedestrian detection and occlusion estimation. In *Proceedings of the European Conference on Computer Vision (ECCV)*. 135–151.